



Ceramic particle-induced accelerated solution-aging behavior of spray-formed 7055 aluminum alloy TIG weld metal

Yun Cheng¹, Wei-xia Yuan¹, Jun-hua Xu^{1,*} , Li-hua Yu¹, Yun-xuan Hu¹, Ting Huang¹, and Hao Zhang¹

¹ School of Materials Science and Engineering, Jiangsu University of Science and Technology, Zhenjiang 212003, China

Received: 20 October 2022

Accepted: 22 December 2022

Published online:

3 January 2023

© The Author(s), under exclusive licence to Springer Science+Business Media, LLC, part of Springer Nature 2023

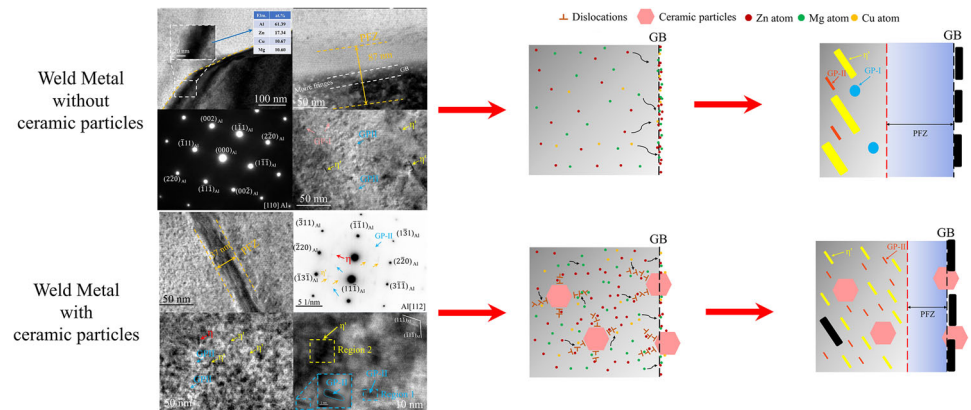
ABSTRACT

The solution-aging behavior and properties of spray-formed 7055 aluminum alloy TIG weld metal (WM) reinforced by TiC–TiB₂ (BC) ceramic particles are investigated, in detail. Weld joints were subjected to solution at 475 °C for 1, 2.5, and 5 h, followed by the aging process at 120 °C for 0–24 h. The results show that ceramic particles not only restrict the grain coarsening of WM during the heat treatment but also accelerate the solution and age-precipitation behavior. The optimum solution time of ceramic particle-reinforced WM is 2.5 h, which has superior aging kinetics due to the completely dissolved eutectic phases. More importantly, during the aging process, ceramic particles decrease the width of the precipitate free zone and modify the size and distribution of precipitates. With the 475 °C/2.5 h + 120 °C/15 h treatment, the tensile strength (530 ± 15 MPa) and elongation (3.9 ± 0.29%) of BC weld joints are higher than 7055 weld joints (358 ± 20 MPa, 2.38 ± 0.42%). Grain refinement, Zener pinning strengthening, coefficients of thermal expansion mismatch strengthening, and precipitation strengthening are the dominant strengthening mechanisms of ceramic particle-reinforced WM.

Handling Editor: Naiqin Zhao.

Address correspondence to E-mail: jhxu@just.edu.cn

GRAPHICAL ABSTRACT



Introduction

Al–Zn–Mg–Cu alloys are widely used in the transportation and aerospace industries because of their ultra-high-strength, outstanding stress corrosion resistance, and high fatigue strength [1–3]. Weldability is essential for making these alloys widely used in production. Unfortunately, due to the notorious hot-crack susceptibility of these alloys, there is no special fusion welding wire available to connect them. Recent studies have found that introducing ceramic particles to the aluminum alloy welding pool can effectively modify the hot-crack susceptibility and enhance the mechanical properties of materials [4–9]. Huang et al. improved the weldability of spray-formed (SF) 7055 aluminum alloy by introducing TiB_2 and ZrB_2 ceramic particles [4–6]. Sokoluk et al. welded 7075 aluminum alloy with $\text{TiC}/7xxx$ filler rods, which not only decreased the hot-crack sensitivity of 7075 aluminum alloy but also greatly improved the mechanical properties of welded joints [7].

However, those studies mentioned above only focused on the as-welded joints. As known, the properties of Al–Zn–Mg–Cu alloys, which are determined by the kind, size, and distribution of precipitates, could be improved by heat treatments [10–12]. Some studies have found that the introduction of ceramic particles can change the heat treatment behavior of aluminum alloys [13–15]. Some reported that ceramic particles accelerated the heat treatment behavior [16, 17], while

others reported that ceramic particles decelerated the heat treatment behavior [18–20].

Xiao et al. found that $\text{TiB}_2/7050$ aluminum matrix composites were more quench sensitive than 7055 alloys due to the dislocations caused by the coefficients of thermal expansion (CTE) mismatch and the high energy interfaces of TiB_2 and $\alpha\text{-Al}$ [13]. Li et al. investigated the aging precipitation of $\text{TiN}/7xxx$ aluminum matrix composites [16]. Compared with the alloys with only Ti or without any refiner, alloys with TiN promoted diffusely uniform precipitation and effectively improved the mechanical properties. Ma et al. found that TiB_2 not only reduced the nucleation energy barrier of precipitation but also accelerated the diffusion of solute atoms and vacancies, thereby accelerating the aging kinetics [17]. However, Pal et al. found that SiC decelerated the aging kinetics of Al–Cu–Mg alloys due to lower vacancies, segregation of alloying elements, and inadequate dislocations [18]. Geng et al. found that TiB_2 gathered along the grain boundaries (GBs) acted as shells to prevent the diffusion of alloying elements and inhabited the dissolution of the second phases, which decelerated the aging kinetics of alloys [19]. Hu et al. found that the formation of MgO in the $\text{B}_4\text{C}/\text{Al}$ interface depleted the Mg atoms and suppressed the precipitation during aging process [20]. Therefore, the effect of ceramic particles on the solution and aging behavior of aluminum alloy has not been determined, which depends on the kinds and content of ceramic particles, alloy composition and other factors.

Some literatures show that weld joints of Al–Zn–Mg–Cu alloys reinforced by ceramic particles preferred to fracture at the weld metal (WM) [4, 7, 21], which indicated that WM was the weakest position of joints. Therefore, appropriate heat treatment parameters can effectively improve the properties of ceramic particle reinforced weld joints. However, there is little research on the solution and aging behavior of 7xxx-WM reinforced by ceramic particles. The effect of TiC–TiB₂ on the solution and aging behavior of SF 7055-WM was further investigated based on [21], which provided a foundation for the heat treatment process of ceramic particles reinforced weld joints.

Experimental

The preparation of TiC–TiB₂/7xxx (BC) filler rods and the weld parameters for SF 7055 aluminum alloy can be found in [21].

The weld joints were solid solution treated at 475 °C for 1, 2.5, and 5 h and being quenching in water at 65 °C. Then these weld joints were artificially aged at 120 °C for 0–24 h, and taken out every 3 h. Metallographic analyses were observed by the optical microscope (Axioskop2-MAT). The phase composition of WM was observed by the X-ray powder diffraction (XRD, Shimadzu XRD-600, Cu K α 1), the scanning range of XRD is 30–80° and the scanning rate is 4°/min. Microstructures and fracture morphologies of WM were observed by the scanning electron microscope (SEM, Gemini SEM 300). The nano-strengthening precipitates of WM were observed by the transmission electron microscope (TEM, JEM-2010F). The microhardness of WM was obtained by the microhardness (MH-5D) tester at 100 g for the duration of 15 s. Based on GB/T 2651-2008, tensile tests were measured by the electronic universal testing machine (CMT 5205) at a drawing speed of 2 mm/min.

Results and discussion

Solution and aging treatment

Solution treatment

The SF 7055 aluminum alloy joints welded with 7055 and BC filler rods were treated with solution

treatment. Figure 1 shows the micrographs of 7055-WM and BC-WM with solution treatment for 1, 2.5, and 5 h (S-0, S-1, S-2.5, and S-5). The microstructure of S-1 7055-WM is coarse dendrites with an average grain size of 115 μ m (Fig. 1a). While the microstructure of S-1 BC-WM is fine equiaxed crystals with a uniform grain size distribution (30 μ m), as shown in Fig. 1d. The grains of S-2.5 7055-WM coarsen into equiaxed crystals with an average grain size of 135 μ m (Fig. 1b). However, the grain growth of S-2.5 BC-WM is not noticeable, and the average grain size is 35 μ m (Fig. 1e). The grain size of S-5 7055-WM continues to grow, and the average grain size is 203 μ m (Fig. 1c). The grain growth of S-5 BC-WM is still not noticeable, and the average grain size is 42 μ m (Fig. 1f). Compared with the dissolution of alloying elements, TiC–TiB₂ ceramic particles could not diffuse during solution treatment, which means ceramic particles can effectively pin the GBs and prevent the migration and growth of GBs, resulting in the grain refinement of WM [16, 22, 23].

Figure 2 shows the SEM and energy dispersive spectroscopy (EDS) images of 7055-WM and BC-WM with different solution times. Based on SEM images of WM, the second phases of WMs are measured by Image J, as shown in Fig. 3.

With the S-1 treatment, the area ratio of second phases in 7055-WM and BC-WM is $4.46 \pm 0.16\%$ and $2.61 \pm 0.17\%$, respectively (Fig. 2a, d). With the S-2.5 treatment, the second phases in 7055-WM grains are almost completely dissolved, while the second phases in GBs still exist partially continuously (Fig. 2b), with an area ratio of $2.16 \pm 0.23\%$. There are no large second phases in the grains and GBs of BC-WM, with area ratios of $1.40 \pm 0.14\%$ (Fig. 2e). According to EDS, the residual eutectic phases are rich in Al–Cu–Mg elements and Al–Cu–Fe elements.

With the S-5 treatment, the second phases of 7055-WM have been significantly dissolved, with an area ratio of $1.35 \pm 0.17\%$ (Fig. 2c), and the area ratio of the second phases in BC-WM is $1.19 \pm 0.14\%$ (Fig. 2f). Although the solution time has doubled, the effect of solution in BC-WM has no longer significantly increased. Therefore, the eutectic phases of BC-WM can be dissolved by S-2.5 treatment. In addition, the content of eutectic phases in S-5 7055-WM is the same as in S-2.5 BC-WM, indicating that ceramic particles can accelerate the solution of alloying elements in WM.

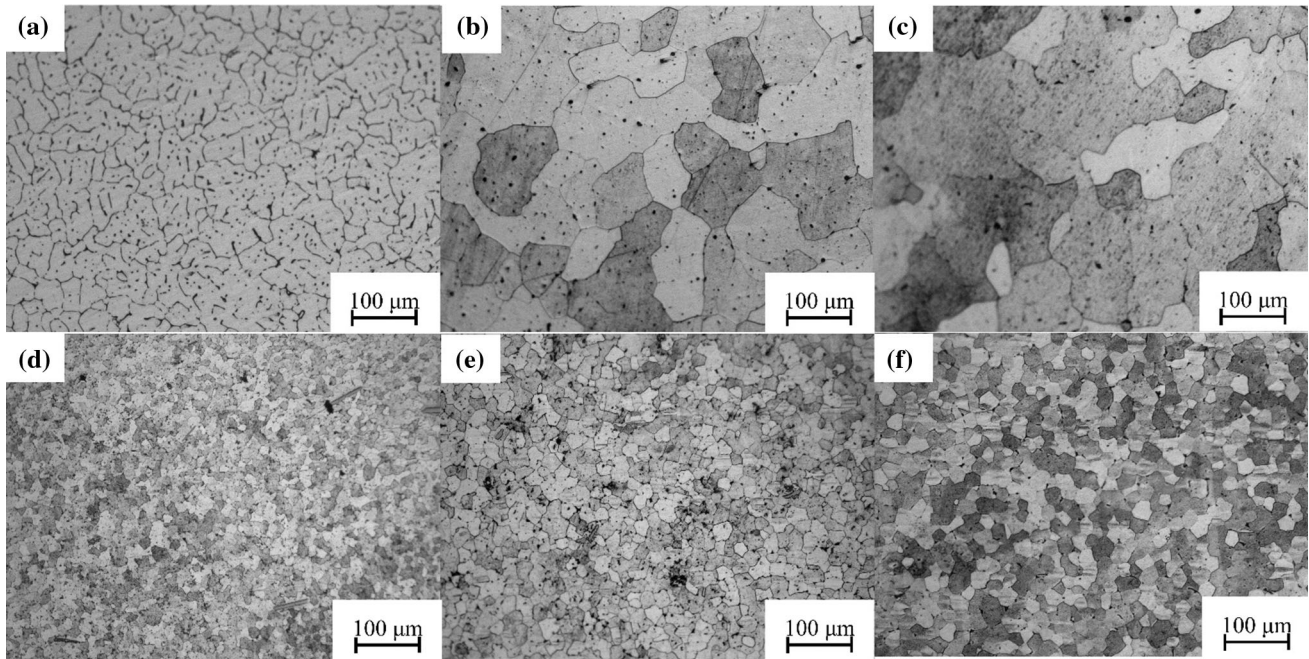


Figure 1 OM images of 7055-WM and BC-WM with different solution times: a–c 7055 S-1, S-2.5 and S-5; d–f BC S-1, S-2.5 and S-5.

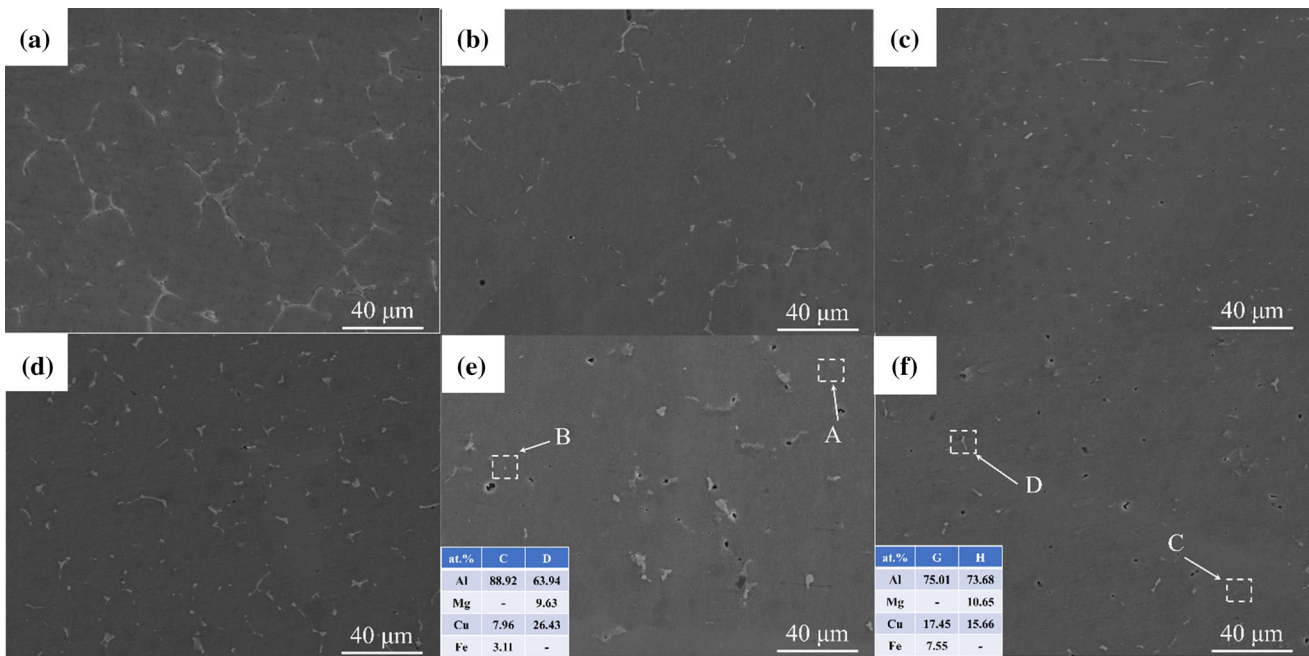


Figure 2 SEM images and EDS of 7055-WM and BC-WM with different solution times: a–c 7055 S-1, S-2.5 and S-5; d–f BC S-1, S-2.5 and S-5.

Figure 4 shows the XRD diffraction patterns of S-2.5 7055-WM and BC-WM. S-2.5 7055-WM is composed of α -Al, $MgZn_2$, and Al_2CuMg , and Al_7Cu_2Fe . S-2.5 BC-WM are mainly composed of α -Al, Al_3Ti , TiC , Al_2CuMg and Al_7Cu_2Fe . According to XRD (Fig. 4) and EDS (Fig. 3), $MgZn_2$ dissolved into the Al

lattice during solution treatment, and the two residual eutectic phases are Al_2CuMg and Al_7Cu_2Fe . These WMs were further treated with S-5, but these residual phases were still residual and could not be completely dissolved (Fig. 2f). The results are consistent with [15, 24, 25].

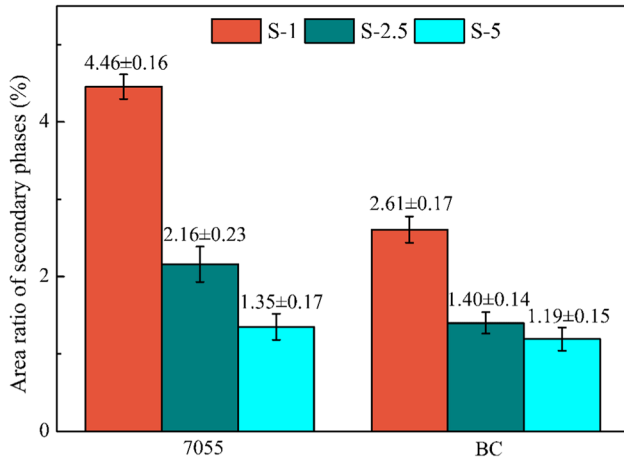


Figure 3 Area ratios of the second phases in 7055-WM and BC-WM with different solution times.

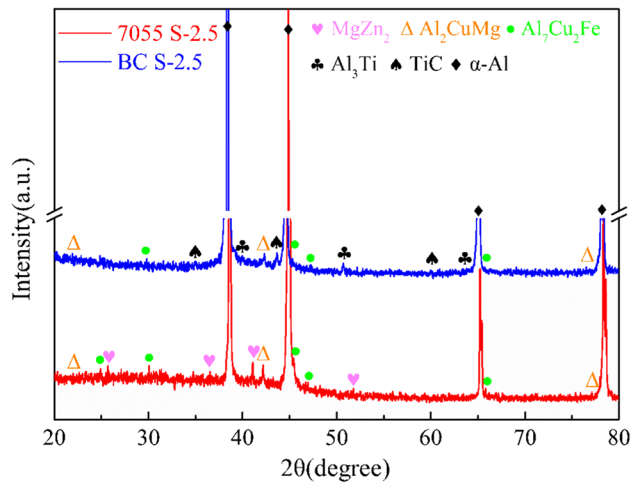


Figure 4 X-ray diffraction pattern of S-2.5 7055-WM and BC-WM.

The relationship between diffusion temperature and time of alloying elements during homogenization can be described as [26]:

$$A(t) = A_0 \exp \left[-\frac{4\pi^2 D_0 t}{L^2} \exp \left(-\frac{Q}{RT} \right) \right] \quad (1)$$

where A_0 is the initial amplitude of the composition segregation, D_0 is the diffusion coefficient, Q is the diffusion activation energy, R is the gas constant, T is the temperature, t is the time of heat treatment, and L is the inter-dendritic spacing.

Equation (1) is used to calculate the theoretical solution time of BC-WM. The diffusion coefficient of Cu is much lower than Mg and Zn at the same temperature. Therefore, the solution process is suggested to be controlled by the diffusion of Cu. The solid

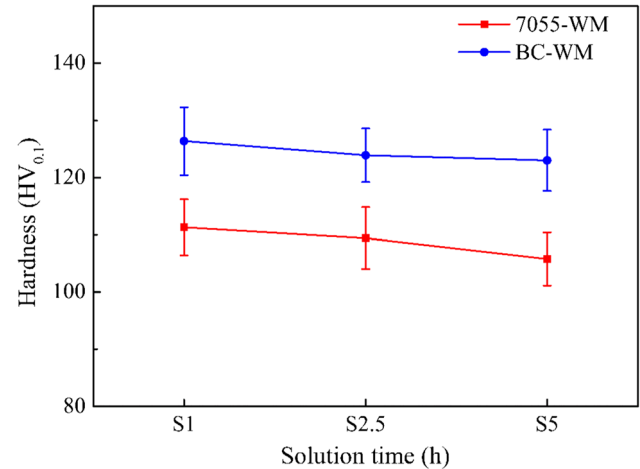


Figure 5 Microhardness of 7055-WM and BC-WM with different solution times.

solubility of Cu in the Al matrix is 5.6%. Assuming the alloying elements are almost completely soluted when the segregation amplitude of Cu is reduced to 5.6%, i.e.:

$$\frac{A(t)}{A_0} = \frac{5.6}{100} \quad (2)$$

then

$$A(t) = A_0 \exp \left[-\frac{4\pi^2 D_0 t}{L^2} \exp \left(-\frac{Q}{RT} \right) \right] \quad (3)$$

By taking natural logarithms of both sides, Eq. (3) can be rewritten as

$$\frac{1}{T} = \frac{R}{Q} \ln \left(\frac{4\pi^2 D_0 t}{2.88 L^2} \right) \quad (4)$$

The average inter-dendritic spacing L of as-welded BC-WM is 26 μm [21], respectively. $D_0(\text{Cu}) = 0.084 \text{ cm}^2/\text{s}$, $Q(\text{Cu}) = 136.8 \text{ kJ/mol}$, $R = 8.314 \text{ J/(mol K)}$, and the solution temperature T is 748 K. By substituting them into Eq. (4), the corresponding solution time is ca. 5 h (4.97 h). However, as shown in the SEM images (Fig. 2) and the area ratios of second phases (Fig. 3), there is no discernible change between the alloying elements of BC-WM with S-2.5 treatment and S-5 treatment, indicating that ceramic particles reduce the solution time of WMs. Both experimental results and theoretical calculations prove that ceramic particles can accelerate the solution of alloying elements.

Figure 5 shows the microhardness of 7055-WM and BC-WM with different solution times. It is found

that at the same solution time, the microhardness of BC-WM is higher than 7055-WM. The microhardness of 7055-WM decreases with increasing solution time, from 111 HV_{0.1}(S-1) to 106 HV_{0.1}(S-5). However, the microhardness of BC-WM barely decreased and remained above 120 HV_{0.1}. The superior microhardness of WM reinforced by ceramic particles was caused by the grain refinement strengthening (Fig. 1), ceramic particles with higher hardness, and the solution strengthening of more alloying elements [16].

Aging treatment

Figure 6 shows the age-hardening curves of 7055-WM and BC-WM (S-1, S-2.5, and S-5). WMs increase rapidly during the initial aging process and then exhibit peak-aging behaviors.

With the S-1 treatment, BC-WM exhibit peak-aging at 18 h, and the microhardness is 203.48 ± 1.27 HV_{0.1}. However, the microhardness of 7055-WM increases consistently during the whole aging process and is 195.24 ± 1.14 HV_{0.1} at 24 h. With the S-2.5 treatment, BC-WM exhibit peak-aging at 15 h, which is 206.86 ± 2.20 HV_{0.1}, and the aging kinetics increase compared to S-1. However, the microhardness of 7055-WM still increases consistently, and is 198.08 ± 2.15 HV_{0.1} at 24 h. With the S-5 treatment, the aging kinetics of BC-WM no longer increase, and exhibit peak-aging at 15 h, which is 204.68 ± 2.62 HV_{0.1} and 205.60 ± 1.36 HV_{0.1}, respectively. However, the aging kinetics of 7055-WM continues to

increase, exhibiting peak-aging at 21 h, which is 198.18 ± 1.55 HV_{0.1}.

It is found that compared with 7055-WM, the microhardness of BC-WM with ceramic particles has faster aging kinetics at the same solution time. The CTE dislocations and the particles/matrix interface could act as the pipe diffusion of alloying elements, accelerating the aging kinetic and shortening the time to peak-aging [17, 27]. By comparing the age-hardening curves of WM under different solution times, with each increasing solution time, the time of WM to peak-aging decreases. The optimal solution time of BC-WM is 2.5 h, in which eutectic phases are almost completely dissolved and possess the best aging kinetics. When the solution time is less than 2.5 h, the eutectic phases of BC-WM dissolve incompletely, and the aging kinetics is insufficient. When the solution time exceeds 2.5 h, the residual eutectic phases could not dissolve anymore, and the aging kinetics could no longer increase.

Tensile properties

Figure 7 shows the stress–strain curves of 7055 and BC weld samples with S-1A-15, S-2.5A-15, and S-5A-15 treatments. Since these specimens all fractured at WM, these values are all the strength of WM, which is consistent with the trend of the age-hardening curves (Fig. 6).

At the same aging time (15 h), the tensile properties of 7055 joints improve with increasing solution time. The tensile strength and ductility of S-5A-15 7055 joints is 397 ± 15 MPa and $2.61 \pm 0.24\%$,

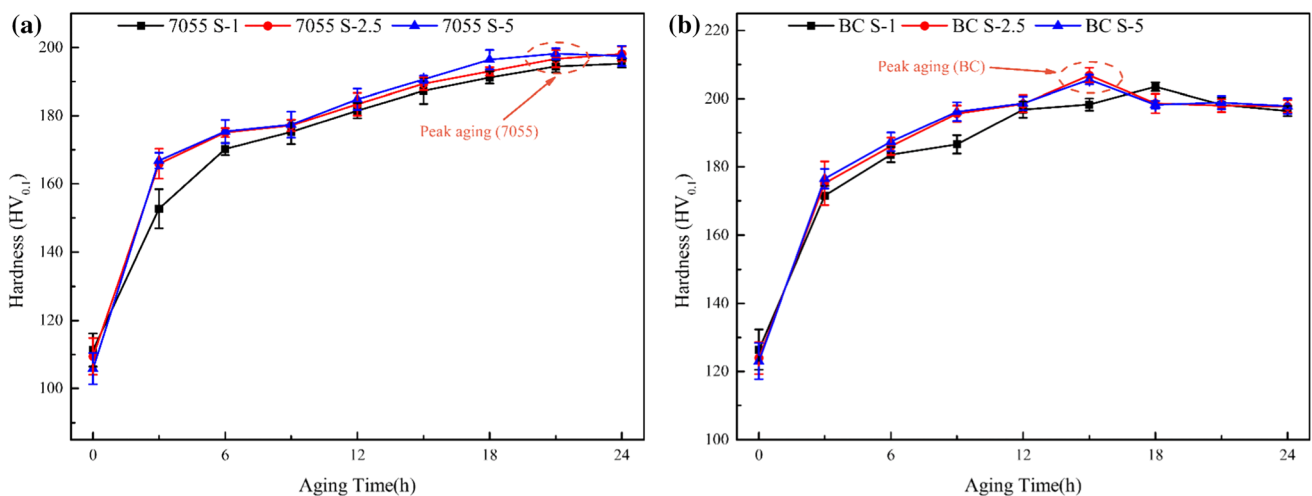


Figure 6 The age-hardening curves of 7055-WM and BC-WM: **a** S-1; **b** S-2.5; **c** S-5.

respectively. However, the tensile properties of BC joints exhibit the peak values with S-2.5A-15 treatment, which are 530 ± 15 MPa, $3.9 \pm 0.29\%$, respectively (S-2.5A-15 7055: 358 ± 16 MPa, $2.38 \pm 0.42\%$). The alloying elements in BC-WM have been nearly completely soluted with S-2.5 treatment. The grains of BC-WM could coarsen with the increasing solution time. Therefore, the tensile properties of BC-WM decreased with the S-5A-15 treatment.

Figure 8 shows the fracture morphologies of S-2.5A-15 7055 and BC joints. The grains of S-2.5A-15

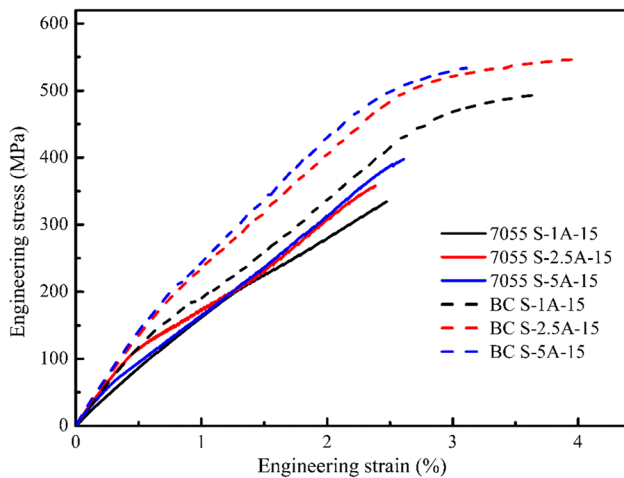


Figure 7 The stress–strain curves of 7055 and BC weld samples with S-1A-15, S-2.5A-15, and S-5A-15 treatment.

7055-WM have continued to grow more than $150 \mu\text{m}$ in the aging process. It can be seen that some second phases exist in the fractures, which are residual eutectic phases from the solution process according to the EDS (Fig. 8a, b) [25]. The eutectic phases in the S-2.5A-15 7055-WM GBs are still partly continuously present, which are the initiations of cracks under load. However, the microstructure of BC-WM is fine equiaxed crystals less than $45 \mu\text{m}$, whose growth is limited by ceramic particles during the aging process (Fig. 8c–e). In addition, the initiation and propagation paths of cracks have also decreased due to the reduction of eutectic phases. Therefore, the strength of BC joints is superior to the 7055 joints with S-2.5A-15 treatment.

Figure 8d, e shows that some dimples with some particles exist in the BC joints. According to the EDS and [25], these submicron particles are Al_3Ti , TiC and TiB_2 , which could enhance the strength of joints by Zener pinning strengthening [28]. Therefore, the tensile strength of the BC joints is better than 7055 joints with S-2.5A-15 treatment.

Analysis of precipitates in aging process

Figure 9 shows the microstructure of ceramic particles in the BC-WM. The diameter of the ceramic particles is ca. $50\text{--}100 \text{ nm}$, as shown in Fig. 9a. Some

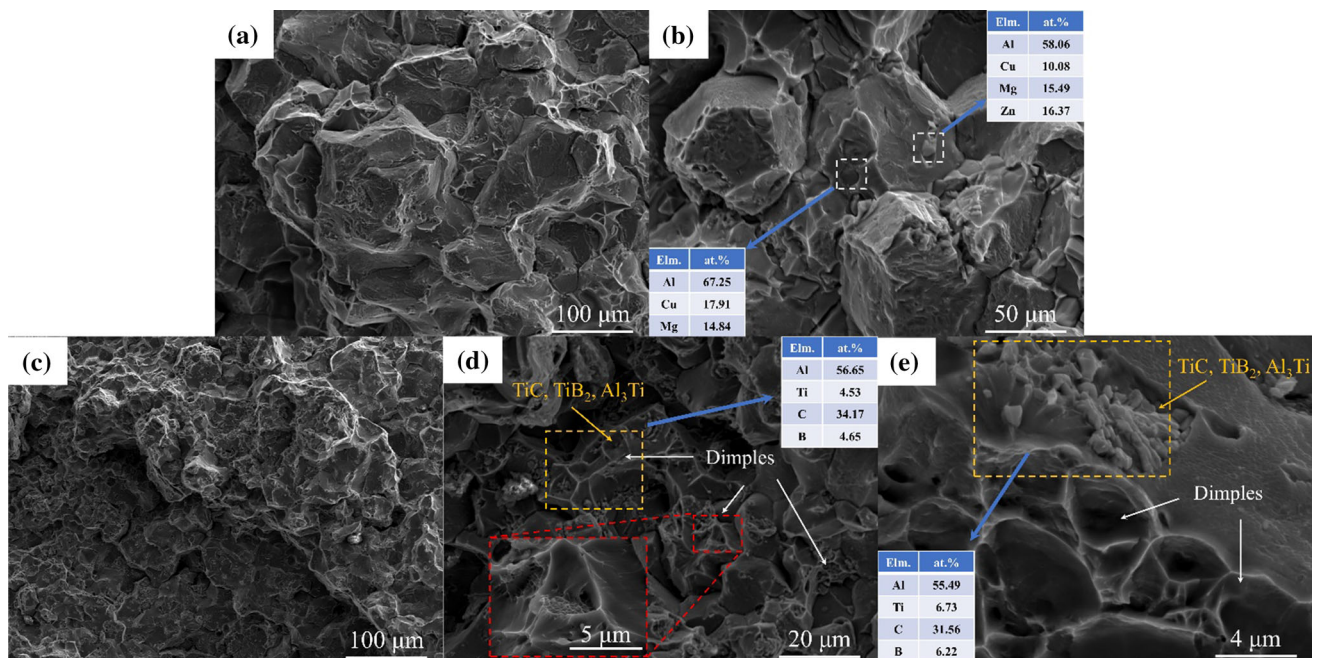
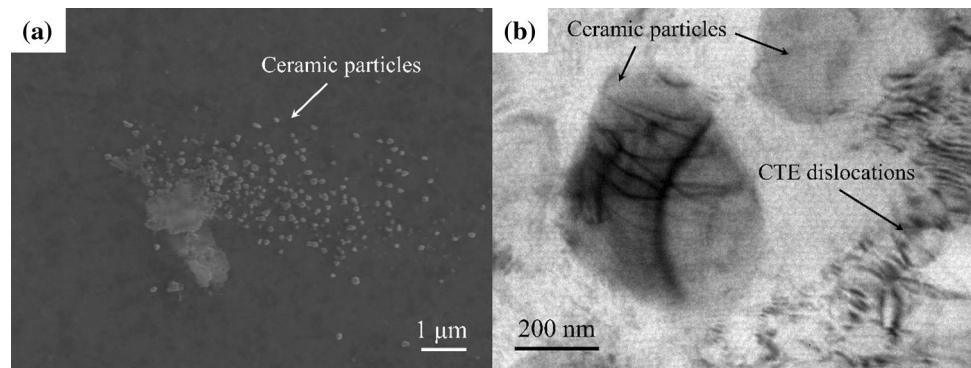


Figure 8 Fracture micrographs of 7055 (a, b) and BC (c–e) joints with S-2.5A-15 treatment.

Figure 9 The SEM image (a) and TEM image (b) of ceramic particles in the BC-WM.



CTE dislocations in the α -Al matrix, around ceramic particles, could accelerate the aging behavior of precipitates, as shown in Fig. 9b. To acknowledge the precipitation behaviors of WM without or with ceramic particles in the aging process more accurately, BC-WM and 7055-WM with S-2.5A-15 were further investigated by TEM analysis.

Figure 10 shows the TEM images of S-2.5A-15 BC-WM. The moiré fringe exists in the BC-WM GBs. The precipitate free zone (PFZ) has a width of 37 nm. The selected area electron diffraction (SAED) pattern of the $[112]_{\text{Al}}$ projection is shown in Fig. 10c. As seen, the diffraction spots of α -Al have been identified. Meanwhile, there are also some weak spots in the SAED pattern, which have been indexed [29–31]. The weak spots located at the $(311)_{\text{Al}}/2$ have been indexed as Guinier–Preston-II (GP-II) zones, as shown by the blue arrows in Fig. 10c [32]. The weak spots located at the $1/3(220)_{\text{Al}}$ and $2/3(220)_{\text{Al}}$ have been indexed as η' phases, as shown by the red arrows in Fig. 10c. The weak spots located at the $(220)_{\text{Al}}/2$ have been indexed as η phases, as shown by the red arrows in Fig. 10c. Therefore, the precipitates of S-2.5A-15 BC-WM are GP-II zones, η' , and η phases. Figure 10d shows the microstructure of precipitates in S-2.5A-15 BC-WM. The precipitates in BC-WM are evenly distributed in the matrix. The length of the η phase is ca. 15 nm and the thickness is ca. 3 nm (Fig. 10d).

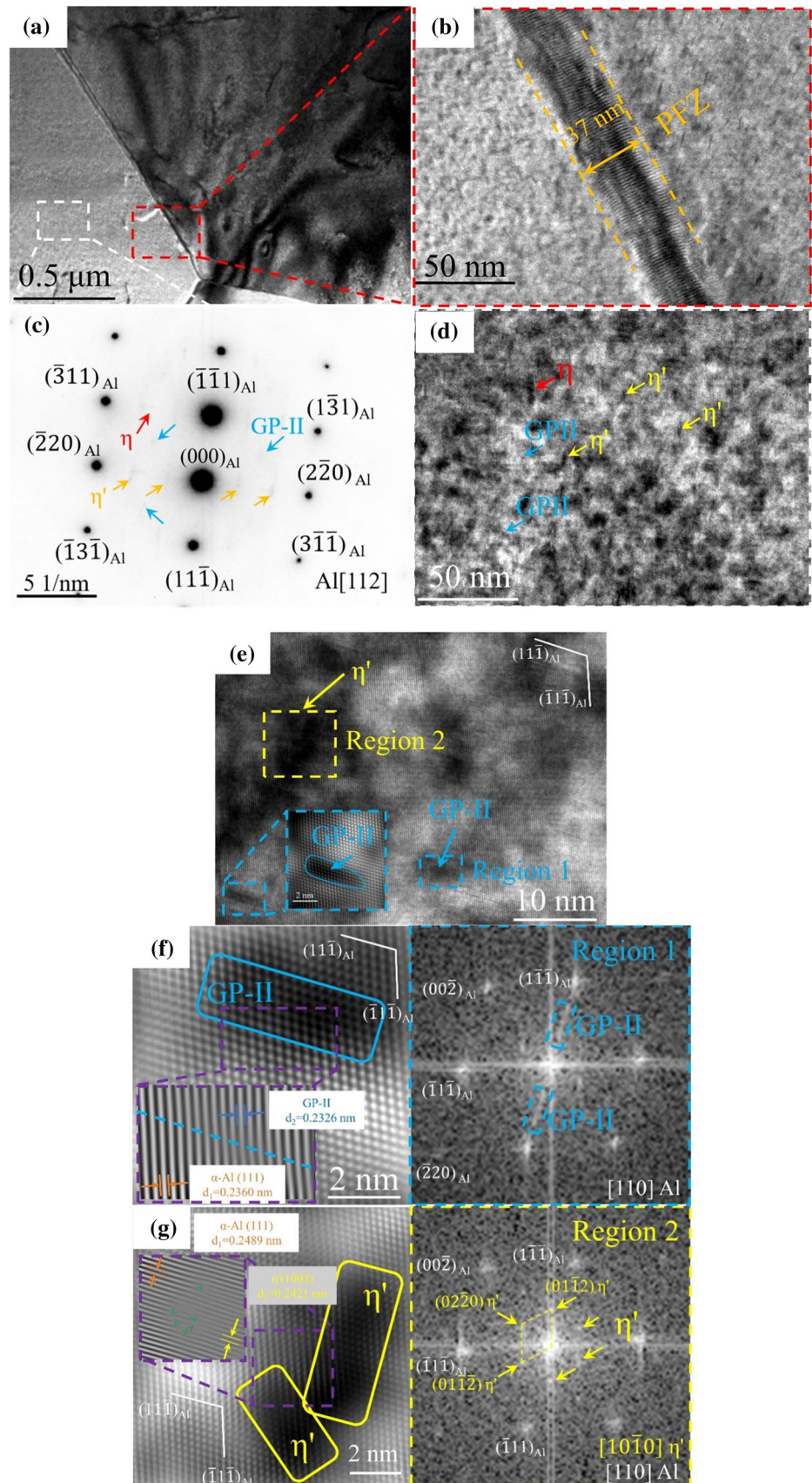
Figure 10e–g shows the high-resolution transmission (HRTEM) images of precipitates in S-2.5A-15 BC-WM. According to the diffraction spots (Fig. 10f, g), the precipitates in the Region 1 and 2 (Fig. 10e) are indexed as GP-II zones and η' phases, respectively [33, 34]. The length of GP-II zones is ca. 4 nm, and the thickness is ca. 1 nm. The length of η' phases is ca. 5–8 nm, and the thickness is ca. 1–3 nm. It can also be found that the η' phases in the Region 2 (Fig. 10e) contact each other and present the trend to coarsen

and grow into η phases, indicating that the over-aging behavior could occur if the aging time continues to increase.

There are two groups of lattice fringes at the GP-II/Al interface, which are 0.2360 nm and 0.2326 nm, corresponding to the $(111)_{\text{Al}}$ and GP-II zones, respectively (Fig. 10f). The well-bonding GP-II/Al interface indicates that the orientation relationship of GP-II zones and α -Al is coherent. As shown in Fig. 10g, there are also two groups of lattice fringes at the η'/Al interface, which are 0.2489 nm and 0.2421 nm, corresponding to $(111)_{\text{Al}}$ and $(1003)_{\eta'}$, respectively. A few dislocations exist at the η'/Al interface, indicating that the orientation relationship of the η' phases and α -Al is semi-coherent. The lattice fringes of $(111)_{\text{Al}}$ are larger than the standard value ($d(111)_{\text{Al}} = 0.2338$ nm), indicating that the lattice of α -Al is distorted [33].

Figure 11 shows the TEM images of S-2.5A-15 7055-WM. The PFZ has not formed in the GBs, indicating S-2.5A-15 7055-WM is still in the early aging process and has not exhibited peak-aging (Fig. 11a) [35]. While the PFZ with a width of 87 nm, wider than that of BC-WM (Fig. 10b), forms in other GBs with the moiré fringe. (Fig. 11b). The SAED pattern of $[110]_{\text{Al}}$ projection is shown in Fig. 11c. There are no weak spots of other phases in Fig. 11c, indicating that few precipitates in S-2.5A-15 7055-WM, which is consistent with Fig. 11d. In addition, the large-size precipitates in S-2.5A-15 7055-WM are unevenly distributed (Fig. 11d). The corresponding FFT diffractograms of these precipitations are shown in Fig. 11e, f. The η' phases with a length of ca. 12–18 nm and a thickness of ca. 2–3 nm exist in the Region 1 of Fig. 11e and Region 3 of Fig. 11f. There are some disk-like precipitates in the Region 2 of Fig. 11e. However, there are no corresponding weak spots in the FFT pattern. This disk-like precipitates are GP-I zones, which is the early aging precipitates

Figure 10 TEM images of S-2.5A-15 BC-WM: **a** morphology characterizations of GBs and the matrix; **b** the PFZ in GBs; **c** the SAED pattern of the matrix; **d, e** the microstructure of precipitates; **f, g** FFT and IFFT diffractograms of the Region 1 and 2.



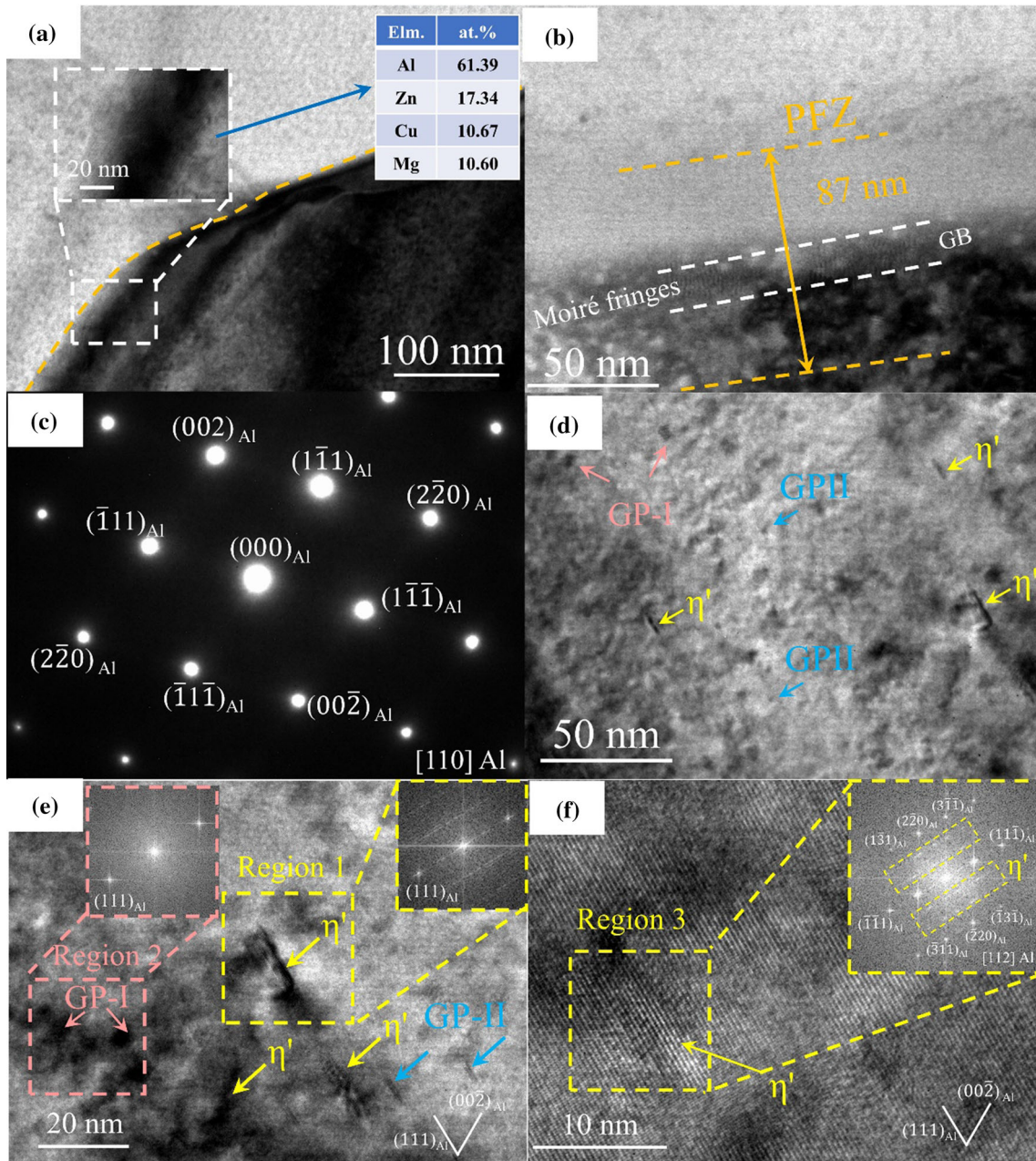


Figure 11 TEM images of S-2.5A-15 7055-WM: **a**, **b** GBs and the PFZ; **c** the SAED pattern of the matrix; **d** the microstructure of precipitates; **e**, **f** HRTEM of precipitates.

of the Al–Zn–Mg–Cu alloys [36]. There are also some GP-II zones with a length of ca. 7 nm and a thickness of ca. 1 nm in Fig. 11e. The number of precipitates in 7055-WM significantly decreases, the size increases, and the distribution is worse.

The precipitation sequence of Al–Zn–Mg–Cu alloys can be described as: GP zones → η′ → η [37, 38]. The η′ (η) phases are the growth phases of GP zones. In the S-2.5A-15 state, the precipitates in BC-WM are

GP-II zones and η′ (η) phases (Fig. 10), and that in 7055-WM are GP-(I/II) zones and η′ phases (Fig. 11). The appearance of η′ (η) phases in BC-WM indicates that ceramic particles promote the aging behavior of precipitates. In addition, the finer and more dispersed precipitates in S-2.5A-15 BC-WM indicate that ceramic particles could modify the age-precipitation behaviors and enhance the mechanical properties.

Discussion

Evolution of precipitates and PFZs in WM during the aging process

Part 3.3 shows the differences in precipitates and PFZs in BC-WM and 7055-WM with S-2.5A-15 treatment, indicating ceramic particles modify the aging-precipitation behaviors. With the S-2.5 treatment, the alloying elements of ceramic particle-reinforced WMs (CRWMs) are almost completely dissolved, while those of 7055-WM are incompletely dissolved. In addition, the dislocations gathered by the CTE mismatch provide the diffusion paths of alloying elements. Therefore, the aging kinetics of CRWMs is faster than that of 7055-WM. Figure 12 shows the evolution of precipitates and PFZs in WM during the aging process.

With the S-2.5 treatment, the residual eutectic phases in 7055-WM GBs are more than CRWMs. Therefore, the alloying elements dissolved in the 7055-WM matrix are less than CRWMs. In addition, the CTE dislocations are formed in the CRWMs matrix (Fig. 12a, b).

In the early aging process, the precipitation behavior is driven by the Gibbs isotherm adsorption decoration, the repartition of solutes occurs between GBs and the matrix [39, 40]. Solute tend to diffuse to the region with more vacancies. GBs, as vacancy sinks, can effectively capture the vacancies generated during solution treatment. Most solutes diffuse into the 7055-WM GBs. In addition, more alloying elements are in the 7055-WM GBs than in the matrix. Therefore, the larger rich-solute clusters form in the 7055-WM GBs, while the smaller rich-solute clusters form in the matrix (Fig. 12c). Although the same diffusion process of solutes occurs in the CRWMs, the CTE dislocations in the matrix, acting as vacancy sinks, can also capture the vacancies during solution treatment [41, 42]. Therefore, there is a competition for adsorbing solutes between GBs and the matrix in the CRWMs. The solutes diffused into CRWMs GBs decrease, while the concentration of solutes in the matrix remains high. Both larger rich-solute clusters form in GBs and the matrix of WMs with ceramic particles (Fig. 12d).

Subsequently, the precipitation behavior is driven by the spinodal decomposition [43–45]. The larger rich-solute clusters enrich the surrounding solutes

and grow into precipitates. However, the smaller rich-solute clusters could not form precipitates and disappear due to the low content of solutes. Since most of the larger rich-solute clusters of 7055-WM exist at GBs, the solutes near GBs dissolve into GBs, which form the wider PFZ. In addition, due to a few larger rich-solute clusters and a relatively short aging time of 7055-WM, these larger clusters could not obtain sufficient solutes. Thus, the precipitates of 7055-WM are GP-(I/II) zones and η' phases (Fig. 12e). In addition, the alloying elements solute in the matrix are few. Thus, the number of precipitates is small, and the size is large.

Compared with the 7055-WM, more large clusters exist in the matrix of CRWMs. The CTE dislocations could also capture solutes and accelerate the aging behavior (Fig. 9). Therefore, solutes near GBs are less likely to diffuse to GBs, resulting in a narrow PFZ. In addition, GP-II zones and η' (η) phases form in the CRWMs. Meanwhile, there is competition for adsorbing solutes among these larger clusters during the aging process. Thus, there are more fine precipitates with a dispersed distribution in the CRWMs (Fig. 12f).

Strengthening mechanism

Compared with 7055-WM, CRWMs have superior mechanical properties with S-2.5A15 treatment, which are mainly strengthened through grain refinement strengthening, Zener pinning strengthening, CTE mismatch strengthening, and precipitation strengthening.

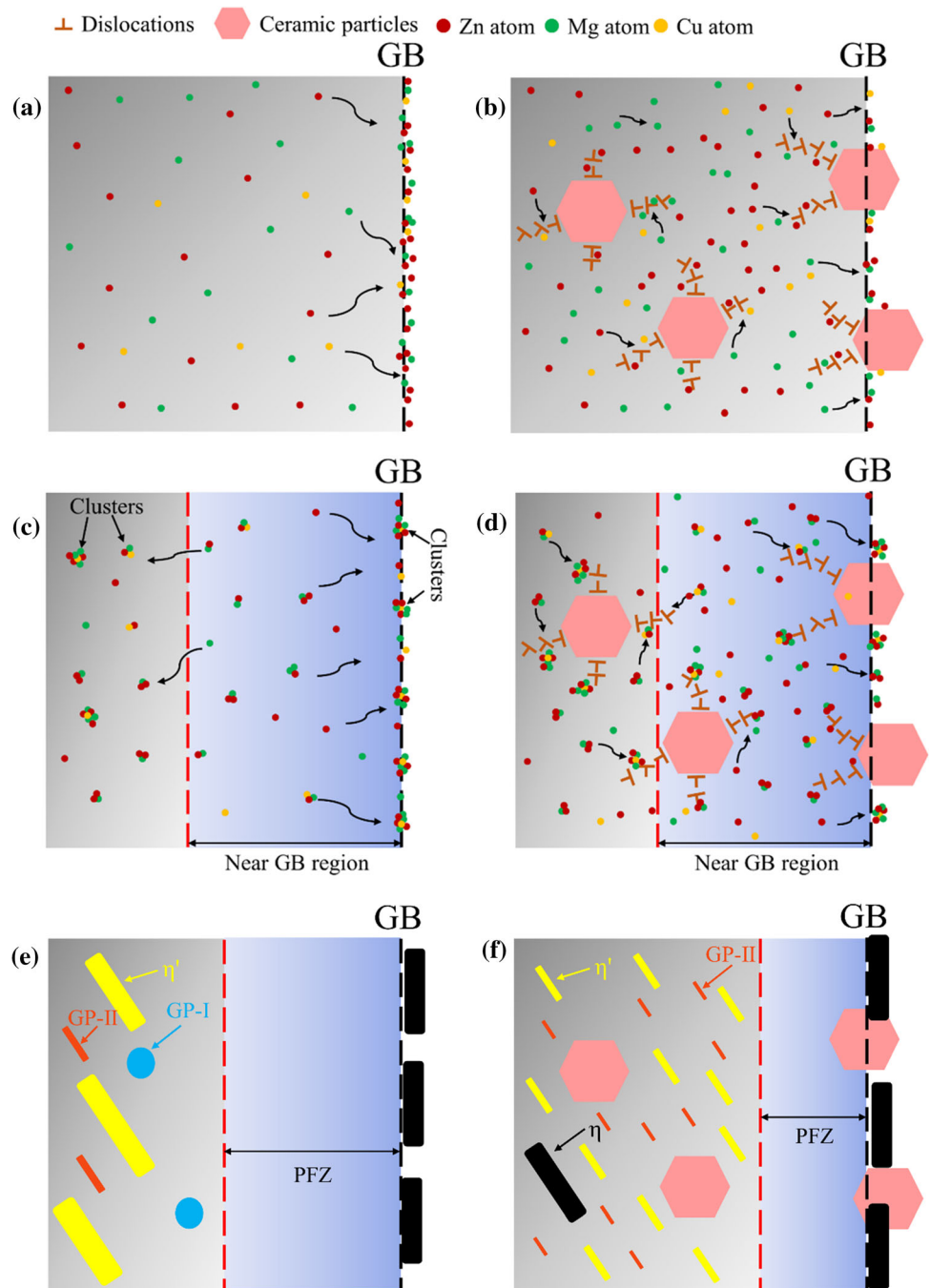
(1) Grain refinement strengthening.

After solution-aging treatment, the CRWMs grains are finer than the 7055-WM coarse grains [23]. The strength increment $\Delta\sigma_H$ [46] caused by the grain refinement is as follows:

$$\Delta\sigma_H = kd^{-1/2} \quad (5)$$

where k is the strengthening constant, and d is the grain size of α -Al. The severe coarsened grains in 7055-WM are more than 150 μm , while the grains in CRWMs are ca. 50 μm , indicating that the grain growth is inhibited by the ceramic particles. Therefore, the mechanical properties of CRWMs could be improved by grain refinement strengthening.

Figure 12 Evolution of precipitates and PFZs in WM without or with ceramic particles during the aging process: **a**, **c**, and **e** without ceramic particles; **b**, **d**, and **f** with ceramic particles.



(2) Zener pinning strengthening.

When the tensile samples are stretched, the load is transferred from the soft phases α -Al to the hard phases submicron TiC, TiB₂, and Al₃Ti. These submicron ceramic particles could pin and hinder the migration of dislocations under load, thereby improving the mechanical properties of CRWMs. The

strength increment $\Delta\sigma_z$ [47] caused by the Zener pinning is as follows:

$$\Delta\sigma_z = (3f\Gamma)/(2r) \tag{6}$$

where Γ is the GBs tension, r is the radius of the pinning particles. The submicron ceramic particles in BC-WM are TiC, TiB₂, and Al₃Ti. As seen from Eq. (7), the improvement in BC-WM strength is

significant as the number of submicron ceramic particles increases.

(3) CTE mismatch strengthening.

When the temperature changes, thermal stress is generated at the particles/matrix interface by the CTE mismatch between particles and α -Al, resulting in distortions of lattices and increasing the resistance to dislocation migration. In addition, the CTE dislocations are also gathered at the particles/matrix interface. Therefore, the mechanical properties of CRWMs could be improved by CTE mismatch strengthening. The strength increment $\Delta\sigma_{CTE}$ [48] is as follows:

$$\Delta\sigma_{CTE} = \eta G b \sqrt{(6\Delta T \Delta C_f) / [b d (1 - f)]} \quad (7)$$

where η is a constant equal 1 [48], G is the elastic shear modulus of the matrix b is the Burgers vector, ΔT is the temperature change from the heat treatment temperature to room temperature (RT), ΔC is the CTE difference between the matrix and ceramic particles. Therefore, the mechanical properties of CRWMs could be effectively improved when the weld joints cool from the aging temperature to RT.

(4) Precipitation strengthening.

Precipitation strengthening [49], which includes the shearing and Orowan strengthening, is the most important strengthening mechanism in Al-Zn-Mg-Cu alloys. When the size of precipitates is small, dislocations could pass them by cutting, and the dominant strengthening mechanism is the shearing strengthening. While the size of precipitates is large, dislocations could not pass them, but bulge between and loop around, and the dominant strengthening mechanism is the Orowan strengthening [50].

The size of GP-II zones and η' phases is small, and the orientation relationships with the matrix are coherent and semi-coherent, respectively [51]. Therefore, dislocations could pass them by shearing. The strength increment $\Delta\sigma_\tau$ [52] caused by shearing strengthening is as follows:

$$\Delta\sigma_\tau = c_1 f^m r_p^n \quad (8)$$

where c_1, m , and n are constants, r_p is the radius of shear precipitates. However, the orientation relationships between the η phases and the matrix is incoherent [35]. Therefore, dislocations bulge between η phases and bypass them. The strength

increment $\Delta\sigma_{or}$ [52] caused by Orowan strengthening is as follows:

$$\Delta\sigma_{or} = c_2 f^{1/2} r^{-1} \quad (9)$$

where c_2 is constant. In this case, the Orowan strengthening decreases with increasing radius of precipitates [52].

For 7055-WM, the precipitates are mainly GP-(I/II) zones and η' phases, with only shearing strengthening [53]. However, the precipitates of BC-WM are GP-II zones, η' , and η phases, indicating that the precipitation strengthening of BC-WM is the coupling of shearing strengthening and Orowan strengthening. In addition, the precipitates in 7055-WM are large and few, which contributes to little strength improvement. However, the precipitates in BC-WM are finer and more numerous, which contributes to a more significant strength improvement. Therefore, the strength of CRWMs is superior to 7055-WM with S-2.5A15 treatment.

Conclusions

- (1) During solution treatment, ceramic particles hinder the grains' coarsening, accelerate the solution behavior, and enhance the microhardness of CRWMs. The optimal solution time of CRWMs is 2.5 h. The eutectic phases are almost completely dissolved, and the aging kinetics of CRWMs is the best.
- (2) During the aging process, ceramic particles accelerate the precipitation behavior of CRWMs, decrease the width of PFZs, and modify the aging behavior of precipitates.
- (3) With the 475 °C/2.5 h + 120 °C/15 h treatment, the tensile strength (530 ± 15 MPa) and ductility ($3.9 \pm 0.29\%$) of the BC joints are high 7055 joints (358 ± 20 MPa, $2.38 \pm 0.42\%$), respectively. The dominant strengthening mechanisms of CRWMs are Grain refinement, Zener pinning strengthening, CTE mismatch strengthening and precipitation strengthening.

Acknowledgements

This work was supported by Graduate Research and Innovation Projects of Jiangsu Province (CN) (KYCX20_3098).

Author Contributions

YC contributed to (First Author) conceptualization, methodology, software, investigation, formal analysis, and writing—original draft; WY contributed to data curation and writing—original draft; JX (Corresponding Author) contributed to conceptualization, funding acquisition, resources, supervision, and writing—review and editing; LY contributed to visualization and investigation; YH contributed to software and validation; TH contributed to visualization and writing; HZ contributed to resources and supervision.

Data and code availability

The raw/processed data required to reproduce these findings cannot be shared at this time as the data also forms part of an ongoing study.

Declarations

Conflict of interest The authors declare that they have no known competing financial interests or personal relationships that could have appeared to influence the work reported in this paper.

Ethical Approval There are no experiments involving human tissue.

References

- [1] Lu Z, Xu J, Yu L, Zhang H, Jiang Y (2022) Studies on softening behavior and mechanism of heat-affected zone of spray formed 7055 aluminum alloy under TIG welding. *J Mater Res Technol* 18:1180–1190. <https://doi.org/10.1016/j.jmrt.2022.03.074>
- [2] Hidalgo MP, Cepeda CM, Orozco A, Ruano OA, Carreño F (2014) Role of particles on microstructure and mechanical properties of the severely processed 7075 aluminium alloy. *J Mater Sci* 49(2):833–841. <https://doi.org/10.1007/s10853-013-7767-x>
- [3] Czerwinski F (2020) Cerium in aluminum alloys. *J Mater Sci* 55(1):24–72. <https://doi.org/10.1007/s10853-019-03892-z>
- [4] Huang T, Xu J, Yu L, Hu Y, Cheng Y, Zhang H (2021) Effect of welding wires containing ZrB₂ particles on microstructure and mechanical properties of spray-formed 7055 aluminum alloy TIG welded joints. *Adv Mater Sci Eng* 2021:1–9. <https://doi.org/10.1155/2021/6953756>
- [5] Huang T, Xu J, Yu L, Hu Y, Cheng Y, Zhang H (2021) Study on ductile fracture of unweldable spray formed 7055 aluminum alloy TIG welded joints with ceramic particles. *Mater Today Commun*. <https://doi.org/10.1016/j.mtcomm.2021.102835>
- [6] Huang T, Xu J, Yu L, Cheng Y, Hu Y, Zhang H (2021) Appropriate amount of TiB₂ particles causes the ductile fracture of the un-weldable spray-formed 7055 aluminium alloy TIG-welded joint. *Mater Res Express*. <https://doi.org/10.1088/2053-1591/ac2194>
- [7] Sokoluk M, Cao C, Pan S, Li X (2019) Nanoparticle-enabled phase control for arc welding of unweldable aluminum alloy 7075. *Nat Commun* 10(1):98. <https://doi.org/10.1038/s41467-018-07989-y>
- [8] Choi H, Cho W-h, Konishi H, Kou S, Li X (2012) Nanoparticle-induced superior hot tearing resistance of A206 alloy. *Metall Mater Trans A* 44(4):1897–1907. <https://doi.org/10.1007/s11661-012-1531-8>
- [9] Cheng Y, Hu Y, Xu J, Yu L, Huang T, Zhang H (2022) Studies on microstructure and properties of TiB₂–Al₃Ti ceramic particles reinforced spray-formed 7055 aluminum alloy fusion welded joints. *J Mater Res Technol* 19:1298–1311. <https://doi.org/10.1016/j.jmrt.2022.05.116>
- [10] Erol M, Kısasöz A, Yaman P, Karabeyoğlu SS, Barut U (2022) A study on high temperature dry sliding wear of AA7050-T4 and effects of the test temperature on microstructure, corrosion behavior, hardness and electrical conductivity. *Mater Today Commun* 31:103410. <https://doi.org/10.1016/j.mtcomm.2022.103410>
- [11] Ayvaz SI, Arslan D, Ayvaz M (2022) Investigation of mechanical and tribological behavior of SiC and B₄C reinforced Al–Zn–Mg–Si–Cu alloy matrix surface composites fabricated via friction stir processing. *Mater Today Commun* 31:103419. <https://doi.org/10.1016/j.mtcomm.2022.103419>
- [12] Pan A, Tzeng C, Bor Y, Liu H, Lee L (2021) Effects of the coherency of Al₃Zr on the microstructures and quench sensitivity of Al–Zn–Mg–Cu alloys. *Materials Today Commun* 28:102611. <https://doi.org/10.1016/j.mtcomm.2021.102611>
- [13] Xiao H, Geng J, Li Y, Li H, Chen D, Wang M, Li Z, Wang H (2021) Microstructure characteristics for quench sensitivity of in-situ TiB₂/7050Al composite. *J Mater Res* 36(6):1341–1356. <https://doi.org/10.1557/s43578-021-00196-4>
- [14] Zhang HB, Wang B, Zhang YT, Li Y, He JL, Zhang YF (2020) Influence of aging treatment on the microstructure and mechanical properties of CNTs/7075 Al composites. *J Alloys Compd* 814:152357. <https://doi.org/10.1016/j.jallcom.2019.152357>
- [15] Lu T, He T, Chen W, Chen H, Liu Y, Wan B, Fu Z, Scudino S (2020) Effect of solution time on the microstructure, precipitation behavior and mechanical properties of (Co0.5N-IFeCrTi0.5 + SiC)p/7075Al hybrid composite. *Mater*

- Character 170:110702. <https://doi.org/10.1016/j.matchar.2020.110702>
- [16] Li X, Cai Q, Zhao B, Liu B, Li W (2018) Precipitation behaviors and properties of solution-aging Al–Zn–Mg–Cu alloy refined with TiN nanoparticles. *J Alloys Compd* 746:462–470. <https://doi.org/10.1016/j.jallcom.2018.02.271>
- [17] Ma Y, Addad A, Ji G, Zhang M-X, Lefebvre W, Chen Z, Ji V (2020) Atomic-scale investigation of the interface precipitation in a TiB₂ nanoparticles reinforced Al–Zn–Mg–Cu matrix composite. *Acta Mater* 185:287–299. <https://doi.org/10.1016/j.actamat.2019.11.068>
- [18] Pal S, Mitra R, Bhanuprasad VV (2008) Aging behaviour of Al–Cu–Mg alloy–SiC composites. *Mater Sci Eng A* 480(1–2):496–505. <https://doi.org/10.1016/j.msea.2007.07.072>
- [19] Geng J, Hong T, Ma Y, Wang M, Chen D, Ma N, Wang H (2016) The solution treatment of in-situ sub-micron TiB₂/2024 Al composite. *Mater Des* 98:186–193. <https://doi.org/10.1016/j.matdes.2016.03.024>
- [20] Hu HM, Lavernia EJ, Harrigan WC, Kajuch J, Nutt SR (2001) Microstructural investigation on B4C/Al-7093 composite. *Mater Sci Eng A* 297(1):94–104. [https://doi.org/10.1016/S0921-5093\(00\)01254-5](https://doi.org/10.1016/S0921-5093(00)01254-5)
- [21] Cheng Y, Xu J, Yu L, Hu Y, Huang T, Zhang H (2021) Effect of TiC/TiC–TiB₂ on microstructure and mechanical properties of spray formed 7055 aluminum alloy TIG welded joints. *J Mater Res Technol* 15:1667–1677. <https://doi.org/10.1016/j.jmrt.2021.08.146>
- [22] Guo B, Song M, Zhang X, Cen X, Li W, Chen B, Wang Q (2020) Achieving high combination of strength and ductility of Al matrix composite via in-situ formed Ti–Al₃Ti core-shell particle. *Mater Character* 170:110666. <https://doi.org/10.1016/j.matchar.2020.110666>
- [23] Chen YD, Li ZC, Dan CY, Chen YC, Wang HW, Wang L, Liu J, Wu Y, Chen Z (2022) Abnormal grain growth in in situ TiB₂ particle-reinforced 7055 Al composites. *J Mater Sci* 57(3):1778–1795. <https://doi.org/10.1007/s10853-021-06635-1>
- [24] Yuan J, Zuo M, Sokoluk M, Yao G, Pan S, Li X (2020) Nanotreating High-Zinc Al–Zn–Mg–Cu Alloy by TiC Nanoparticles, Springer International Publishing 318–323. Doi: https://doi.org/10.1007/978-3-030-36408-3_46
- [25] Wang Z, Wang M, Li Y, Xiao H, Chen H, Geng J, Li X, Chen D, Wang H (2021) Effect of pretreatment on microstructural stability and mechanical property in a spray formed Al–Zn–Mg–Cu alloy. *Mater Des* 203:109618. <https://doi.org/10.1016/j.matdes.2021.109618>
- [26] Liu XY, Pan QL, Fan X, He YB, Li WB, Liang WJ (2009) Microstructural evolution of Al–Cu–Mg–Ag alloy during homogenization. *J Alloys Compd* 484(1–2):790–794. <https://doi.org/10.1016/j.jallcom.2009.05.046>
- [27] Legros M, Dehm G, Arzt E, Balk TJ (2008) Observation of giant diffusivity along dislocation cores. *Science* 319(5870):1646–1649. <https://doi.org/10.1126/science.1151771>
- [28] Mao D, Meng X, Xie Y, Yang Y, Xu Y, Qin Z, Chang Y, Wan L, Huang Y (2022) Strength-ductility balance strategy in SiC reinforced aluminum matrix composites via deformation-driven metallurgy. *J Alloys Compd* 891:162078. <https://doi.org/10.1016/j.jallcom.2021.162078>
- [29] Berg LK, Gjønnes J, Hansen V, Li XZ, Knutson-Wedel M, Waterloo G, Schryvers D, Wallenberg LR (2001) GP-zones in Al–Zn–Mg alloys and their role in artificial aging. *Acta Mater* 49(17):3443–3451. [https://doi.org/10.1016/S1359-6454\(01\)00251-8](https://doi.org/10.1016/S1359-6454(01)00251-8)
- [30] Wang F, Gong Y, Du Y, Song M (2020) Microstructures and mechanical properties of an Al–Zn–Mg–Cu alloy processed by two-step aging treatment. *J Mater Eng Perform* 29(7):4404–4411. <https://doi.org/10.1007/s11665-020-04980-x>
- [31] Bendo A, Matsuda K, Lee S, Nishimura K, Nunomura N, Toda H, Yamaguchi M, Tsuru T, Hirayama K, Shimizu K, Gao H, Ebihara K, Itakura M, Yoshida T, Murakami S (2018) Atomic scale HAADF-STEM study of η' and η1 phases in peak-aged Al–Zn–Mg alloys. *J Mater Sci* 53(6):4598–4611. <https://doi.org/10.1007/s10853-017-1873-0>
- [32] Wei S, Wang R, Zhang H, Xu C, Wu Y, Feng Y (2021) Influence of Cu/Mg ratio on microstructure and mechanical properties of Al–Zn–Mg–Cu alloys. *J Mater Sci* 56(4):3472–3487. <https://doi.org/10.1007/s10853-020-05438-0>
- [33] Jiang Y, Zhao Y, Zhao Z, Yan K, Ren L, Du C (2020) The strengthening mechanism of FSWed spray formed 7055 aluminum alloy under water mist cooling condition. *Mater Character* 162:110185. <https://doi.org/10.1016/j.matchar.2020.110185>
- [34] Chung TF, Yang YL, Huang BM, Shi Z, Lin J, Ohmura T, Yang JR (2018) Transmission electron microscopy investigation of separated nucleation and in-situ nucleation in AA7050 aluminium alloy. *Acta Mater* 149:377–387. <https://doi.org/10.1016/j.actamat.2018.02.045>
- [35] Wang W, Pan Q, Wang X, Sun Y, Ye J, Lin G, Liu S, Huang Z, Xiang S, Wang X, Liu Y (2020) Non-isothermal aging: a heat treatment method that simultaneously improves the mechanical properties and corrosion resistance of ultra-high strength Al–Zn–Mg–Cu alloy. *J Alloys Compd* 845:156286. <https://doi.org/10.1016/j.jallcom.2020.156286>

- [36] Guo R, Zhang C, Liu M, Zhang Z, Chen L, Zhao G (2020) Influence of isothermal and non-isothermal aging treatments on microstructure and properties of Al–Zn–Mg alloy helical profile. *Mater Character* 169:110613. <https://doi.org/10.1016/j.matchar.2020.110613>
- [37] Won SJ, So H, Kang L, Oh SJ, Kim K-H (2021) Development of a high-strength Al–Zn–Mg–Cu-based alloy via multi-strengthening mechanisms. *Scripta Mater* 205:114216. <https://doi.org/10.1016/j.scriptamat.2021.114216>
- [38] Guo W, Guo J, Wang J, Yang M, Li H, Wen X, Zhang J (2015) Evolution of precipitate microstructure during stress aging of an Al–Zn–Mg–Cu alloy. *Mater Sci Eng A* 634:167–175. <https://doi.org/10.1016/j.msea.2015.03.047>
- [39] Lejcek P (2010) Grain boundary segregation in metals. *Springer Ser Mater Sci*. <https://doi.org/10.1007/978-3-642-12505-8>
- [40] Faul Kner R G (2008) Grain boundaries in creep-resistant steels. *Creep-Resistant Steels* 329–349. Doi: <https://doi.org/10.1533/9781845694012.2.329>.
- [41] Fischer FD, Svoboda J, Appel F, Kozeschnik E (2011) Modeling of excess vacancy annihilation at different types of sinks. *Acta Mater* 59(9):3463–3472. <https://doi.org/10.1016/j.actamat.2011.02.020>
- [42] Serrano GD, Pelegrina JL, Condó AM, Ahlers M (2006) Helical dislocations as vacancy sinks in β phase Cu–Zn–Al–Ni alloys. *Mater Sci Eng A* 433(1):149–154. <https://doi.org/10.1016/j.msea.2006.06.040>
- [43] Shen K, Yin ZM, Wang T (2008) On spinodal decomposition in ageing 7055 aluminum alloys. *Mater Sci Eng A* 477(1):395–398. <https://doi.org/10.1016/j.msea.2007.05.049>
- [44] Alhamidi A, Edalati K, Horita Z, Hirosawa S, Matsuda K, Terada D (2014) Softening by severe plastic deformation and hardening by annealing of aluminum–zinc alloy: significance of elemental and spinodal decompositions. *Mater Sci Eng A* 610:17–27. <https://doi.org/10.1016/j.msea.2014.05.026>
- [45] Zhao H, De Geuser F, Kwiatkowski da Silva A, Szczepaniak A, Gault B, Ponge D, Raabe D (2018) Segregation assisted grain boundary precipitation in a model Al–Zn–Mg–Cu alloy. *Acta Mater* 156:318–329. <https://doi.org/10.1016/j.actamat.2018.07.003>
- [46] Gong X, Cao Z, Zeng M, Zou X, Yang Y, Yan H (2022) Effect of aging treatment on the microstructure and mechanical properties of TiO₂@CNTs/2024 composite. *J Mater Sci* 57(35):16675–16689. <https://doi.org/10.1007/s10853-022-07708-5>
- [47] Varanasi RS, Gault B, Ponge D (2022) Effect of Nb microalloying on austenite nucleation and growth in a medium manganese steel during intercritical annealing. *Acta Mater* 229:117786. <https://doi.org/10.1016/j.actamat.2022.117786>
- [48] Wu C, Ma K, Wu J, Fang P, Luo G, Chen F, Shen Q, Zhang L, Schoenung JM, Lavernia EJ (2016) Influence of particle size and spatial distribution of B4C reinforcement on the microstructure and mechanical behavior of precipitation strengthened Al alloy matrix composites. *Mater Sci Eng A* 675:421–430. <https://doi.org/10.1016/j.msea.2016.08.062>
- [49] Li J, Ju J, Zhang Z, Zhou Y, Luo Y, Mudi K, Xie Y, Wang M, Liang J, Wang J (2021) Precipitation behavior and mechanical properties of Al–Zn–Mg–Cu matrix nanocomposites: effects of SiC nanoparticles addition and heat treatment. *Mater Character* 172:110827. <https://doi.org/10.1016/j.matchar.2020.110827>
- [50] Peng X, Li Y, Liang X, Guo Q, Xu G, Peng Y, Yin Z (2018) Precipitate behavior and mechanical properties of enhanced solution treated Al–Zn–Mg–Cu alloy during non-isothermal ageing. *J Alloys Compd* 735:964–974. <https://doi.org/10.1016/j.jallcom.2021.161933>
- [51] Wang H, Xu W, Lu H, Liu Y (2022) Effect of microstructure inhomogeneity on creep behavior of friction stir welding 7B50-T7451 aluminum alloy thick plate joint. *Mater Character* 193:112292. <https://doi.org/10.1016/j.matchar.2022.112292>
- [52] Liu Y, Jiang D, Li B, Yang W, Hu J (2014) Effect of cooling aging on microstructure and mechanical properties of an Al–Zn–Mg–Cu alloy. *Mater Des* 57:79–86. <https://doi.org/10.1016/j.matdes.2013.12.024>
- [53] Xu W, Wang H, Lu H, Liu Y, Dong J (2021) Effect of thermal exposure on microstructure and mechanical properties of friction stir welding 7B50-T7451 aluminium alloy thick plate joint. *J Mater Res Technol* 15:6415–6433. <https://doi.org/10.1016/j.jmrt.2021.11.082>

Publisher's Note Springer Nature remains neutral with regard to jurisdictional claims in published maps and institutional affiliations.

Springer Nature or its licensor (e.g. a society or other partner) holds exclusive rights to this article under a publishing agreement with the author(s) or other rightsholder(s); author self-archiving of the accepted manuscript version of this article is solely governed by the terms of such publishing agreement and applicable law.